ROYAL SOCIETY
OF CHEMISTRY

Check for updates

A polymeric α-tetrasubstituted Co(II)-phthalocyanine catalyst for stable and selective electrochemical carbon dioxide reduction

Kornkamol Mangmoon,[a] Permsak Chairat,[a] Yijiao Jiang, [ID][b] Poobodin Mano,[c] Supawadee Namuangruk [ID][c] and Patchanita Thamyongkit [ID] *[a]

The development of efficient molecular catalysts for electrochemical CO_2 reduction (ECO_2R) remains a key challenge for scalable carbon utilization. Herein, we report the synthesis and electropolymerization of an α-tetraamino-substituted Co(II)-phthalocyanine monomer (**CoPc-1α**) to yield robust polymer films (**p(CoPc-1α)**) on various conductive substrates. The resulting films were characterized by UV-visible spectrophotometry, Raman and attenuated total reflection-Fourier transform infrared (ATR-FTIR) spectroscopy, scanning electron microscopy (SEM) equipped with energy dispersive X-ray spectroscopy (EDX), variable frequency square-wave voltammetry (VF-SWV), and density functional theory (DFT), confirming successful polymer network formation *via* phenazine linkages and efficient electron transfer across macrocyclic units. In H-cell electrolysis at −1.15 V *vs.* NHE, a **p(CoPc-1α)**-modified carbon paper electrode exhibited high selectivity for CO generation with a faradaic efficiency (FE_{CO}) of 97%, along with a current density of 3.8 mA cm^{-2} and a turnover number (TON_{CO}) and a turnover frequency (TOF_{CO}) of 6.0×10^4 and 0.37 s^{-1}, respectively, over 45 h. At an applied potential of −1.54 *vs.* NHE in a flow-cell system, the **p(CoPc-1α)** film on a microporous layer of a carbon fiber paper exhibited remarkable catalytic performance, achieving an average current density of 151 mA cm^{-2} with 98% FE_{CO} for 42 h, corresponding to a TON_{CO} of 1.9×10^6 and a TOF_{CO} of 12.6 s^{-1}. This study demonstrates that **p(CoPc-1α)** offered a balanced profile of high selectivity, long-term stability and practical current output, establishing it as a promising material for scalable CO_2-to-CO conversion.

1. Introduction

Achieving the net-zero greenhouse gas emission goal has become a global agenda driving the development of low-carbon technologies. Among these, carbon dioxide (CO_2) conversion offers a sustainable approach to mitigate climate change while producing value-added chemicals and fuels. Electrochemical CO_2 reduction (ECO_2R) enables conversion of CO_2 by using electricity from renewable energy sources into various chemicals, such as carbon monoxide (CO), methane (CH_4), and formic acid (HCOOH), depending on types of electrocatalysts employed.[1,2] ECO_2R offers several advantages, including mild operating conditions, tunable reaction rates and product selectivity *via* applied potential, and broad scalability.[2–4] To overcome kinetic and thermodynamic barriers associated with the reduction of the inert CO_2 molecule,

the use of an efficient catalyst is very necessary.[5] Metallophthalocyanines (MPcs) have demonstrated high efficiency as electrocatalysts for ECO_2R.[6] Among them, Co(II)-phthalocyanine (CoPc) is widely recognized as one of the most active MPc-based catalysts for ECO_2R.[7–10] Several studies reported the use of monomeric CoPc-modified electrodes, but they suffered from limited stability under operating conditions, often leading to catalyst degradation.[11] To address this, binders, such as polystyrene[12] and Nafion,[13] have been commonly used to immobilize the catalyst onto the electrode substrate and improve film stability. Nonetheless, these binders have been reported to adversely impact catalytic performance by blocking active sites, limiting electron conductivity, causing microstructural destruction and impeding mass transport. Moreover, binder degradation under working conditions could deteriorate film stability.[14–16] To address these limitations, the direct polymerization of CoPc monomers on the electrode surfaces has become a promising option. Among various techniques, electropolymerization stands out as a highly effective method for producing reproducible, uniform thin films with tunable thickness, morphology and orientation in a single step.[17–19] By this process, polymeric CoPc films can be prepared from suitably

[a] *Department of Chemistry, Faculty of Science, Chulalongkorn University, Bangkok, 10330, Thailand. E-mail: patchanita.v@chula.ac.th*

[b] *School of Engineering, Macquarie University, NSW, 2109, Sydney, Australia*

[c] *National Nanotechnology Center (NANOTEC), National Science and Technology Development Agency (NSTDA), Pathum Thani, 12120, Thailand*
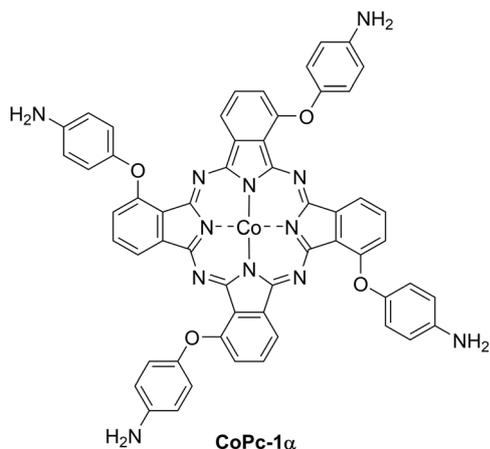
This journal is © the Owner Societies 2026

Phys. Chem. Chem. Phys., 2026, **28**, 3915–3928 | 3915

Fig. 1 A structure of a target monomer.

functionalized monomers containing electropolymerizable groups, such as pyrrole,[20] thiophene[21] or aniline.[22] The substitution patterns on MPc molecules are known to have a significant influence on their electronic and physical properties. Recently, our group reported polymeric ECO_2R catalysts based on β-tetrasubstituted CoPc bearing bithiophenyl,[23] amino[24] and 4-aminophenoxy[25] groups that exhibited outstanding catalytic activity, selectivity and stability. According to previous studies, α-substitution on Pc macrocycles substantially suppressed cofacial π to π association relative to β-substitution, and induced out of plane distortion, thereby reducing aggregation tendency and preserving the exposure of the catalytic sites during the electrolysis.[26] Moreover, α-functionalization could induce greater changes in the physical, optical and electronic properties than β-substitution.[27–30] Building upon these findings, this work aims to synthesize an α-aminophenoxy-tetrasubstituted CoPc monomer (**CoPc-1α**, Fig. 1) and prepare its corresponding electropolymer (**p(CoPc-1)**). Electrochemical properties, charge transfer behavior and electrocatalytic performance of **p(CoPc-1α)** toward heterogeneous ECO_2R in both H-type and flow electrochemical cells were investigated, with a focus on improving catalytic selectivity, productivity and stability.

2. Results and discussion

2.1 Monomer synthesis and polymer film preparation

Synthesis of **CoPc-1α** was carried out via a three-step process following previously published procedures,[31–33] starting from a nucleophilic aromatic nitro displacement reaction of 3-nitrophthalonitrile with 4-nitrophenol in dimethylformamide (DMF) at 60 °C for 24 h, leading to 3-(4-nitrophenooxy)phthalonitrile (**1**) containing a newly formed ether linkage in 92% yield (Scheme 1). Cyclotetramerization of **1** in the presence of Co(OAc)₂·4H₂O and 1,8-diazabicyclo[5.4.0]undec-7-ene (DBU) in dimethylethanolamine (DMAE) under reflux for 4 h resulted in 1,8,15,22-tetra(4-nitrophenoxy)phthalocyaninatocobalt(ɪɪ) (**CoPc-2α**) in 46%. Then, a nitro-reduction of **CoPc-2α** with a mixture of $SnCl_2$ in concentrated HCl and ethanol at room temperature for 20 h gave **CoPc-1α** in
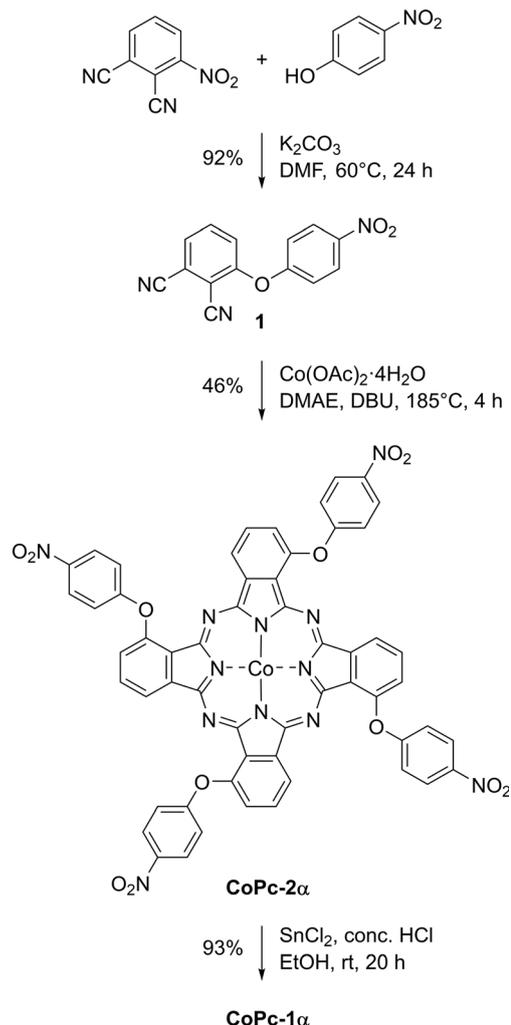
Scheme 1 Synthesis of **CoPc-1α**.

93% yield. Formation of **CoPc-2α** and **CoPc-1α** was confirmed by their molecular ion peaks at m/z 1119.1291 and 999.2314 in high-resolution matrix-assisted laser desorption/ionization time-of-flight (HR-MALDI-TOF) mass spectra.

CoPc-1α was coated on various types of substrates, namely indium tin oxide-coated glass (ITO-glass), gold-coated glass (Au-glass), carbon paper (CPs) and a microporous layer of the commercial carbon fiber paper (MPL-CFP), by means of cyclic voltammetry (CV). Electropolymerization was performed in a 0.1 M tetrabutylammonium hexafluorophosphate (TBAPF₆) solution in DMF containing 0.1 mM **CoPc-1α** in a three electrode one-compartment cell consisting of the ITO-glass, Au-glass, CP or MPL-CFP as a working electrode (WE), an AgCl-coated Ag wire (Ag/AgCl) as a quasi-reference electrode (QRE), and a Pt wire as a counter electrode (CE). A potential range of −0.33 V to 1.27 vs. normal hydrogen electrode (NHE) was applied at a scan rate of 50 mV s^{-1}. Fig. 2 presents the cyclic voltammograms collected during the electropolymerization of **CoPc-1α** on the CP substrate. In the anodic scans, the oxidation of the primary amine group of **CoPc-1α** was observed at 0.89 V vs. NHE and gave the corresponding radical cation, initiating
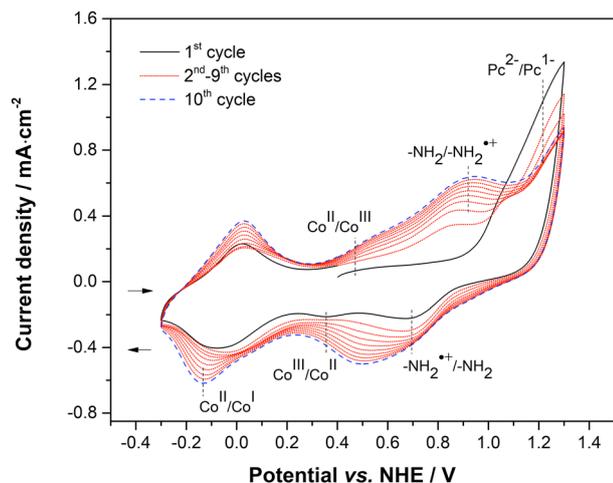
3916 | *Phys. Chem. Chem. Phys.*, 2026, **28**, 3915–3928

This journal is © the Owner Societies 2026

Fig. 2 The cyclic voltammograms of the electrochemical polymerization of **CoPc-1α** on the CP. Black solid, red dotted and blue dashed lines represent the first, the intermediate and the last scanning cycles, respectively.

the electropolymerization.[34,35] The characteristic anodic signals of Co^{II}/Co^{III}, $-NH_2/-NH_2^{•+}$ and Pc^{2-}/Pc^- oxidation were detected at 0.44 V, 0.89 V and 1.19 V *vs.* NHE, respectively.[3] On the reverse scan, the Co^{II}/Co^{I} reduction peak was observed at −0.16 V *vs.* NHE.[36,37] Upon increasing the scanning cycles, the anodic peaks shifted toward more positive potentials and the cathodic ones toward more negative potentials, consistent with the growth of the polymer film on the electrode, which increased the ohmic (iR) drop and amplified the potential shifts.[34,38] In addition, the progressive increase in the anodic peak current of the $-NH_2-NH_2^{•+}$ couple corroborated the continuous polymer deposition on the electrode.[36]

2.2 Polymer film characterization and electrochemical behavior study

Formation of the resulting polymer films of **CoPc-1α** (**p(CoPc-1α)**) was confirmed by UV-visible (UV-vis) spectrophotometry, attenuated total reflection-Fourier transform infrared (ATR-FTIR) spectroscopy, Raman spectroscopy and scanning electron microscopy (SEM) equipped with energy dispersive X-ray spectroscopy (EDX). The UV-vis spectrum of the **p(CoPc-1α)** film on the ITO-glass (**p(CoPc-1α)**/ITO-glass) showed a broad B-band at 363 nm, and Q-bands at 643 and 716 nm, corresponding to those observed from a **CoPc-1α** solution in DMF (**CoPc-1α**/DMF) and a dropcast **CoPc-1α** film on the ITO-glass (**CoPc-1α**/ITO-glass) as shown in Fig. 3a. Peak broadening and slightly red-shifted absorption observed in
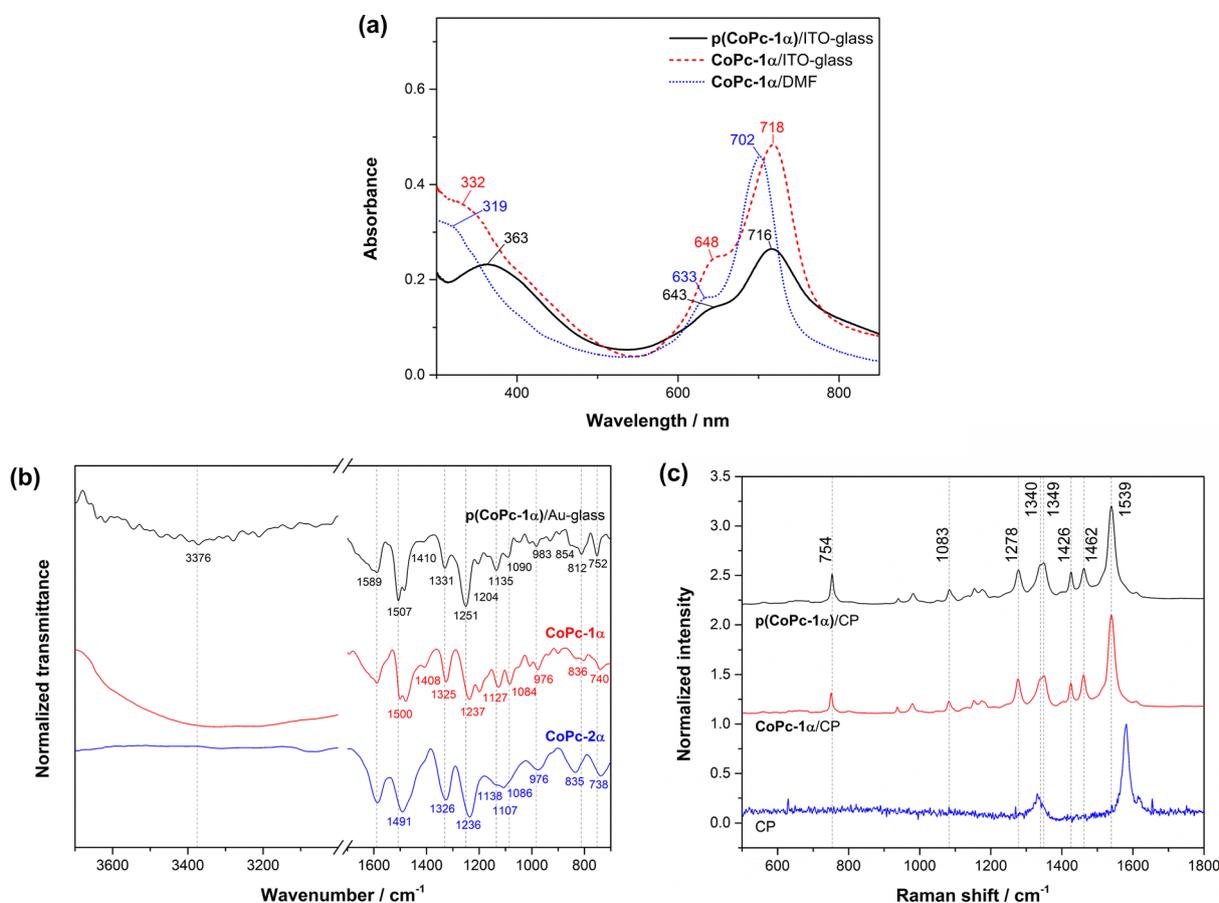

Fig. 3 (a) UV-vis spectra of **p(CoPc-1α)**/ITO-glass (black solid line), **CoPc-1α**/ITO-glass (red dashed line) and **CoPc-1α**/DMF (blue dotted line); (b) ATR-FTIR spectra of **p(CoPc-1α)**/Au-glass (black line), **CoPc-1α** powder (red line) and **CoPc-2α** powder (blue line); and (c) Raman spectra of **p(CoPc-1α)**/CP (black line), **CoPc-1α**/CP (red line) and CP (black line).

p(CoPc-1α)/ITO-glass and **CoPc-1α**/ITO-glass, compared to the absorption of **CoPc-1α**/DMF, was attributed to H-aggregation among the Pc macrocycles in the polymer film.[39–42] As shown in Fig. 3b and Table S1 (SI), the ATR FT-IR spectrum of the **p(CoPc-1α)** film on the Au-glass (**p(CoPc-1α)**/Au-glass) was collected and compared with those of **CoPc-1α** and **CoPc-2α**. The **p(CoPc-1α)** film exhibited C–O–C stretching peaks at 854, 1090 and 1251 cm^{-1},[43–47] C–C stretching vibration peaks of pyrrole and isoindole units at 1331 and 1410 cm^{-1},[43,48] and macrocyclic C=C stretching peaks at 1507 and 1589 cm^{-1}.[43] These signals were consistent with those observed in **CoPc-1α** and **CoPc-2α**, and with those of their β-substituted derivatives (**CoPc-1β**), described in our previous study.[25] Attenuation of the N–H stretching signal in the range of 3000–3600 cm^{-1},[49,50] together with appearance of a peak of phenazine (PNZ) ring vibration with the C–H out-of-plane at 752 cm^{-1} and a skeletal deformation peak at 812 cm^{-1} indicate the possible formation of PNZ bridges within the **p(CoPc-1α)** network.[51] The Raman spectrum of **p(CoPc-1α)**/CP exhibits a similar peak pattern to that of **CoPc-1α**/CP with slightly broader features (Fig. 3c and Table S2, SI). The signals at 754 and 1340 cm^{-1} were assigned to Co–N stretching coupled with pyrrole ring expanding,[52] and C–H in-plane bending and isoindole vibration,[52] respectively. The peaks at 1083 and 1278 cm^{-1} were also attributed to C–H in-plane bending.[53] The vibration peak at 1349 cm^{-1} was a characteristic feature of the Pc ring and corresponded to the C_β–C_β, C_α–C_β–C_β, C_γ–C_δ and C_β–C_γ stretching of the pyrrole group,[54] with an additional C_β–C_β stretching signal found at 1462 cm^{-1}.[55] A peak at 1426 cm^{-1} was assigned to C–N_m–C stretching (where N_m is an N atom coordinated with a Co center) accompanied by pyrrole expanding,[55] while the one at 1539 cm^{-1} corresponded to C–N_m–C stretching together with pyrrole expanding coupled with C–H in-plane bending.[52] Unlike the Raman profiles of the electropolymer of **CoPc-1β** (**p(CoPc-1β)**) reported in our previous work,[25] a distinct feature of the PNZ linkage could not be clearly observed by this technique. SEM-EDX showed uniform Co distribution across the substrate surface with minor local agglomerates, suggesting that **p(CoPc-1α)** was deposited over the entire CP substrate (Fig. S8, SI).

Furthermore, the electrochemical behavior of the **p(CoPc-1α)** film was characterized by CV in a one-compartment three-electrode electrochemical cell consisting of **p(CoPc-1α)**/CP as the WE, Ag/AgCl (saturated KCl) as the reference electrode (RE) and a Pt wire as the CE. 0.1 M KOH solution in deionized water was used as the electrolyte to clearly observe the characteristic redox responses of electrochemically active components in the polymer film, while suppressing interference from oxygen reduction and water splitting reactions.[56,57] The potential was scanned between −0.90 V and 0.40 V vs. NHE at a scan rate of 100 mV s^{-1} as shown in Fig. 4a. During the cathodic sweep, the resulting cyclic voltammogram of the **p(CoPc-1α)**/CP exhibited reduction peaks corresponding to the Co^{II}/Co^{I} and Pc^{2-}/Pc^{3-} couples at −0.27 V and −0.44 V vs. NHE, respectively. These peaks were correlated with those observed in its monomer solution (Fig. S9, SI), thereby indicating the presence of electrochemically active centers for the ECO$_2$R in the **p(CoPc-1α)** film. Furthermore, a prominent reduction peak assigned to the two-electron reduction of the PNZ linkage was observed at −0.08 V vs. NHE. These three reduction peaks were consistent with those described for the β-substituted analog in our previous report.[25] To investigate electron transfer behavior of the above-mentioned electrochemically active components in the **p(CoPc-1α)** film, variable frequency square-wave voltammetry (VF-SWV) was subsequently conducted in the same electrochemical setup, following the previous works.[25,56,57] The charge transfer kinetics of the **p(CoPc-1α)**/CP was investigated by recording 76 SWV curves within a potential window between −1.00 V and 0.20 V vs. NHE across frequencies (f) from 0.33 Hz to 1250 Hz, corresponding to log(f) values between −0.5 and 3.0. As shown in Fig. 4b, the **p(CoPc-1α)** film exhibited the main responses corresponding to the Co^{II}/Co^{I} and Pc^{2-}/Pc^{3-} reductions at the potentials of −0.28, and −0.41 V vs. NHE, respectively. In addition, the highest intensity response of the PNZ linkage appeared at a potential of −0.06 V vs. NHE,
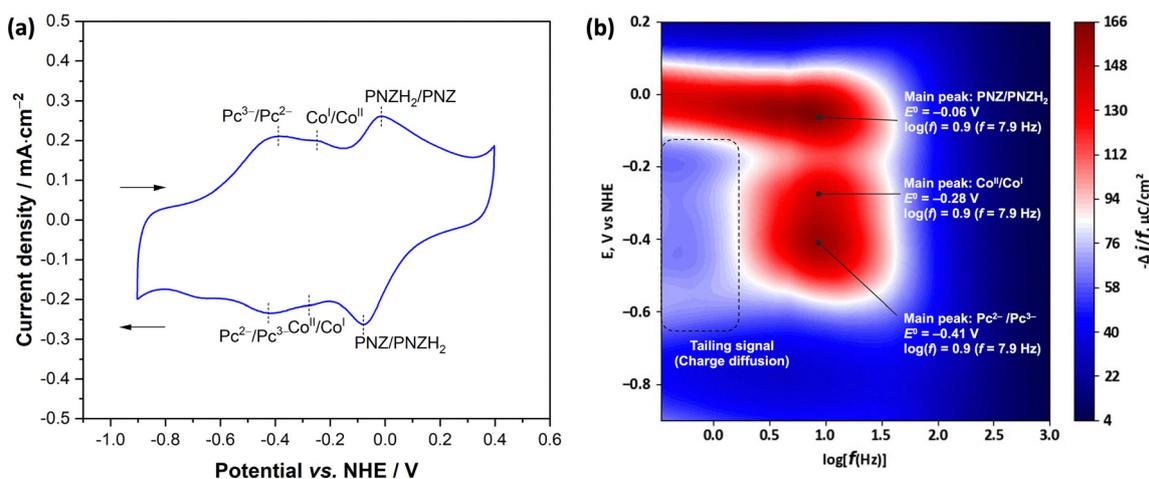

Fig. 4 (a) Cyclic voltammogram and (b) experimentally recorded VF-SWV colormaps of **p(CoPc-1α)**/CP, based on 76 square wave voltammograms collected with pulse times from 0.4 μs to 1.5 s, or the frequencies (f) from 1250 to 0.33 Hz in the region corresponding to Co^{II}/Co^{I} and Pc^{2-}/Pc^{3-} reduction processes.

3918 | Phys. Chem. Chem. Phys., 2026, **28**, 3915–3928

This journal is © the Owner Societies 2026

consistent with the PNZ/PNZH$_2$ reduction peak observed in Fig. 4a. In terms of the frequency response that directly depends on the electron transfer rate in the polymer film, **p(CoPc-1α)**/CP displayed a wide range of frequency responses between the log(f) of 2.2 and −0.40 by exhibiting the major responses of the Co metal center, Pc ring and PNZ linkage at the log(f) of 0.90 (f = 7.9 Hz) with the tail-like response diffused into the lower log(f) of −0.4 (f = 0.4 Hz). These features were originated from charge penetration from the first layer to the bulk catalyst layers as proposed for the β-substituted analog in our previous works. These observations confirmed the formation of a PNZ-conjugated CoPc network from the oxidative electropolymerization of **CoPc-1α** and indicated that the intermacrocyclic electron transfer was facilitated by the newly formed PNZ bridge in the **p(CoPc-1α)** film.

2.3 Electrocatalytic performance

2.3.1 Study on p(CoPc-1α)-catalyzed ECO$_2$R in a H-type electrochemical cell. The electrocatalytic activity of **p(CoPc-1α)** in a batch ECO$_2$R process was evaluated in a two-compartment three-electrode H-type electrochemical cell consisting of cathodic and anodic chambers separated from each other by a Nafion membrane (Fig. S10, SI).[23] **p(CoPc-1α)**/CP and Ag/AgCl (3M KCl) were placed in the cathodic chamber as the WE and RE, respectively, while a Pt wire served as the CE in the anodic chamber. An aqueous solution of 0.5 M KHCO$_3$ was used as the electrolyte in both chambers. As shown in Fig. 5, the CV measurement in the potential range from 0.20 V to −1.20 V vs. NHE with a scan rate of 50 mV s^{-1} under the N$_2$- and CO$_2$-saturated conditions revealed that **p(CoPc-1α)**/CP under the CO$_2$-saturated conditions showed lower reduction potential onset ($E_{red,onset}$), i.e. −0.86 V compared to −0.95 V vs. NHE, and higher current density than that recorded under the N$_2$ saturation. This observation suggested the possible catalytic activity of **p(CoPc-1α)** for ECO$_2$R in the potential range −0.86 V vs. NHE and above. Negligible current density observed from the bare CP confirmed no participation or interference of the CP substrate under the measurement conditions.

After that, controlled potential electrolysis (CPE) was performed at various potentials, starting from −0.80 V to −1.35 V vs. NHE with 0.05 V increments, for 2 h at each potential. The formation of headspace gas products was analyzed via gas chromatography (GC), while the dissolved species were investigated via nuclear magnetic resonance (NMR). Fig. 6a–c show that no significant product formation was detected until the potential of −0.90 V vs. NHE, consistent with $E_{red,onset}$ observed in the above-mentioned CV experiment. Upon increasing the applied potential from −0.90 V to −1.20 V vs. NHE, CO was detected as a sole product with Faradaic efficiency of the CO formation (FE$_{CO}$) increasing from 58% to 94% and the average current density increasing from 1.3 mA cm^{-2} to 7.6 mA cm^{-2}. At −1.25 V to −1.30 V vs. NHE, CO remained the only detectable product, but the current density was unstable despite comparable FE$_{CO}$, likely due to the partial detachment of the **p(CoPc-1α)** film from the substrate. This effect was more pronounced at −1.35 V vs. NHE, where the FE$_{CO}$ dropped to 61% and hydrogen (H$_2$) was generated at 13% FE. According to GC analysis, the CO
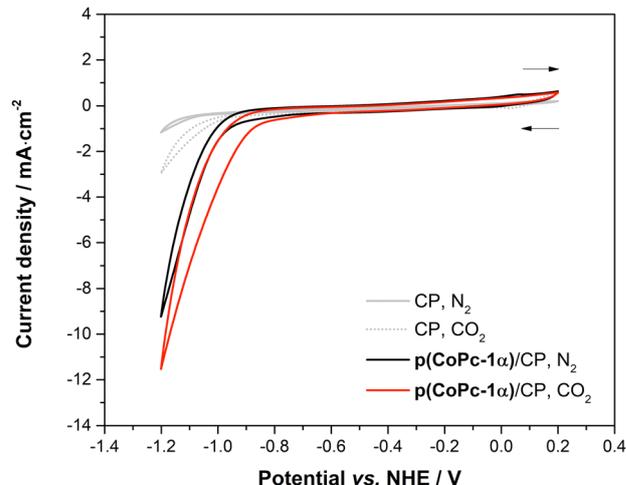

Fig. 5 Cyclic voltammograms of **p(CoPc-1)**/CP under N$_2$- (black solid line) and CO$_2$-saturated conditions (red solid line), compared with those of the bare CP under the N$_2$- (grey solid line) and CO$_2$-saturated conditions (grey dashed line).

production reached up to 7.6 mL in the 2-h interval at an applied potential of −1.25 V vs. NHE and then drastically inclined when the reduction potential was increased further. Based on these results, the reduction potentials of −1.15 V and −1.20 vs. NHE were selected for further stability studies, which will be described later.

The stability of **p(CoPc-1α)** was evaluated at the selected potentials of −1.15 V and −1.20 V vs. NHE under the ECO$_2$R conditions used for the CPE. The results showed that at −1.20 V vs. NHE, **p(CoPc-1α)**/CP gave CO as the sole product at the FE$_{CO}$ above 90% in the first 20 h with the gradually decreasing current density (Fig. S11, SI). After that, the FE$_{CO}$ dropped to 63% after the 40th hour and then to 56 at the 45th hour, when the experiment was terminated. The average current density and the accumulated CO amount were 4.4 mA cm^{-2} and 79.5 mL, respectively. At −1.15 V vs. NHE, the current density and the FE$_{CO}$ were quite stable at approximately 3.8 mA cm^{-2} and 97%, respectively, for at least 45 h with a comparable accumulated CO amount, i.e. 75.1 mL, to that obtained from the ECO$_2$R at −1.20 V vs. NHE (Fig. 6d–e). According to inductively coupled plasma-optical emission spectroscopy (ICP-OES), total catalyst loading of the **p(CoPc-1α)** film on the CP was determined to be 52 nmol cm^{-2} (Table S3, SI). Therefore, for the 45-h ECO$_2$R at −1.15 V vs. NHE, the turnover number (TON$_{CO}$) and a turnover frequency of the CO formation (TOF$_{CO}$) were calculated to be 6.0 × 10^4 and 0.37 s^{-1}, respectively

Interestingly, although **CoPc-1α** and **CoPc-1β** shared structural similarities, **p(CoPc-1α)** exhibited a higher FE$_{CO}$ (97% vs. 94%) at slightly less negative potential than **p(CoPc-1β)** (−1.15 V vs. −1.19 V, vs. NHE). However, **p(CoPc-1β)** clearly outperformed **p(CoPc-1α)** in terms of the current density (5.9 vs. 3.8 mA cm^{-2}) and long-term operational stability (120 h vs. 45 h) (Table S4, SI). The lower TOF$_{CO}$ observed for **p(CoPc-1α)** (0.37 vs. 1.1 s^{-1}) was likely attributed to higher catalyst loading on the CP (52 vs. 25 nmol cm^{-2}), as a result of
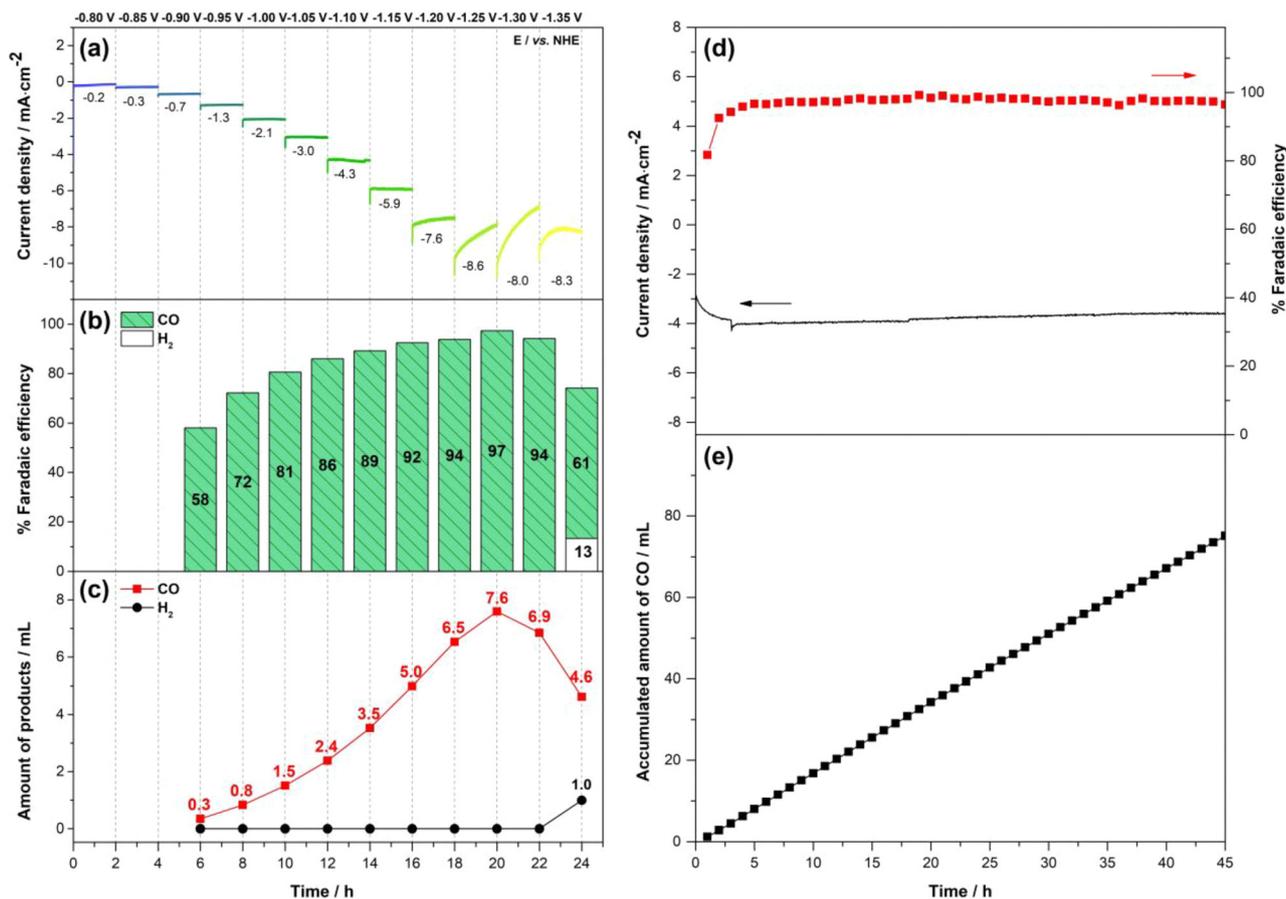
Fig. 6 (a) Chronoamperometric responses, (b) % FE of gas product formation and (c) accumulated amounts of CO (red line) and H_2 (black line) observed in each 2-h interval at various potentials; and (d) chronoamperometric responses with % FE_{CO} and (e) accumulated amount of CO recorded at −1.15 V vs. NHE over 45 h for the **p(CoPc-1α)**-catalyzed ECO_2R in the H-cell.

greater solubility of **CoPc-1α**, compared to that of **CoPc-1β**. This higher loading led to a thicker catalyst film, which might hinder CO_2 diffusion to the active sites close to the electrode surface where electron transfer was most efficient. The weaker frequency-dependent Co^{II}/Co^I feature in the above-mentioned VF-SWV response of the **p(CoPc-1α)**/CP, compared with that of the previously studied **p(CoPc-1β)**/CP,[25] suggested the slower charge transfer kinetics at the Co center in **p(CoPc-1α)**. This observation further supported that the effective turnover was limited by interfacial and interlayer charge transport, and mass transport within the thicker **p(CoPc-1α)** film. Such charge transfer kinetics could also be governed by the local interfacial ion environment and electric double layer structure, which modulated interfacial charge transfer and consequently electrocatalytic rates.[58] Furthermore, electrochemical impedance spectroscopy (EIS) of the **p(CoPc-1α)** films prepared by CV with cycle numbers of 10, 20, and 30 showed a clear increase in the Nyquist plot semicircle size with increasing cycle number (Fig. S12, SI). This trend indicated higher charge transfer resistance and greater transport limitation in the thicker films from higher deposition cycles, thereby reducing the ECO_2R performance. While mechanistic insight was addressed in a later section, these EIS and VF SWV results suggested that the

charge transport across the interface and the mass transport within the catalyst film were key contributors to the lower TOF in the thicker films.[59] Moreover, when compared to other catalyst architectures, such as the previously reported bithiophenyl-substituted CoPc polymer[23] and CoPc-based covalent organic frameworks (COFs),[60,61] **p(CoPc-1α)** exhibited superior product selectivity and operational durability, despite showing lower intrinsic activity, i.e. TOF_{CO}, than the COF-based materials. This study supported that **p(CoPc-1α)**/CP was the stable and effective WE for the batch ECO_2R process. However, due to low solubility of CO_2 in aqueous solution and diffusion-limited current in the H-cell, we extended our study to a continuous ECO_2R using a gas diffusion electrode (GDE), allowing direct feed of gaseous CO_2 to the catalyst surface and enabling rigorous evaluation of activity, selectivity, and durability under practical conditions, as described in the next section.

2.3.2 Study on p(CoPc-1α)-catalyzed ECO₂R in a flow-type electrochemical cell. In this study, the catalytic performance of **p(CoPc-1α)** in the continuous ECO_2R process was investigated by using a custom-built two-compartment three electrode flow-type electrochemical cell, as described in our previous work.[24] The cathodic chamber contained **p(CoPc-1α)**-coated MPL-CFP (**p(CoPc-1α)**/MPL-CFP) and Ag/AgCl (saturated KCl) that served

3920 | *Phys. Chem. Chem. Phys.*, 2026, **28**, 3915–3928

This journal is © the Owner Societies 2026

as the WE and RE, respectively. The Pt wire was used as the CE and located in the anodic chamber that was separated from the cathodic one by an anion exchange membrane (AEM). An N_2- or CO_2-saturated aqueous solution of 1.0 M $KHCO_3$ was pumped into both compartments at a flow rate of 15 mL min^{-1}. The cyclic voltammogram of **p(CoPc-1α)**/MPL-CFP recorded between 0.20 V and −1.50 V *vs.* NHE at a scan rate of 50 mV s^{-1} showed lower $E_{red,onset}$ under the CO_2 saturation, −0.60 V *vs.* NHE, than that under the N_2-saturated conditions, −0.70 V *vs.* NHE, with higher current density at more negative potential (Fig. S13, SI). Under both conditions, the bare MPL-CFP also exhibited current enhancement at the reduction potential higher than −0.90 V *vs.* NHE due to the H_2 formation. These observations indicated potential catalytic activity of the **p(CoPc-1α)**/MPL-CFP for the continuous ECO_2R process. A CPE study was hence conducted to evaluate the catalytic performance of the **p(CoPc-1α)**/MPL-CFP at various reduction potentials, starting from −0.97 V to −1.73 V *vs.* NHE for 2 h at each potential as shown in Fig. 7a–c. The current density was first detected at −0.97 V *vs.* NHE and CO was obtained at 65% FE as the sole product. As the potential was stepped to more negative, the current density, %FE$_{CO}$ and CO production were all increased. At 1.73 V *vs.* NHE, H_2 evolution was observed and the experiment was not continued further.

Although, at −1.62 V *vs.* NHE, the FE$_{CO}$ and CO amount reached 100% and 118 mL, respectively, the current signal was relatively noisy. Therefore, the subsequent stability test was performed at −1.54 V *vs.* NHE, where the %FE and the CO production were still high, *i.e.* 98% and 98 mL, respectively, and the current density level was comparatively steady.

Fig. 7d and e show that by using the **p(CoPc-1α)**/MPL-CFP as the GDE in the flow cell, the ECO_2R at −1.54 V *vs.* NHE exhibited stable current density approximately 140 mA cm^{-2} in the first 20 h. After that, the current density slightly increased and became stable again at approximately 160 mA cm^{-2} by the 25th hour before drastically dropping after the 42th hour due to electrolyte leakage from the cell. Over 42 h, the ECO_2R in this flow cell was highly productive with average FE$_{CO}$ of 98% and the accumulated CO amount of 2.84 L with the average current density of 151 mA cm^{-2}. Accordingly, TON$_{CO}$ and TOF$_{CO}$ were enhanced to 1.9×10^6 and 13 s^{-1}, respectively, compared with the ECO_2R in the H-cell. According to the SEM-EDX analyses, the **p(CoPc-1α)**/MPL-CFP before and after the electrolysis appeared similar, showing uniform catalyst distribution and the expected existence of carbon, oxygen and cobalt atoms (Fig. S14, SI). The increase in the current density and the subsequent electrolyte leakage arose from hydroxide (OH^-) generation during the
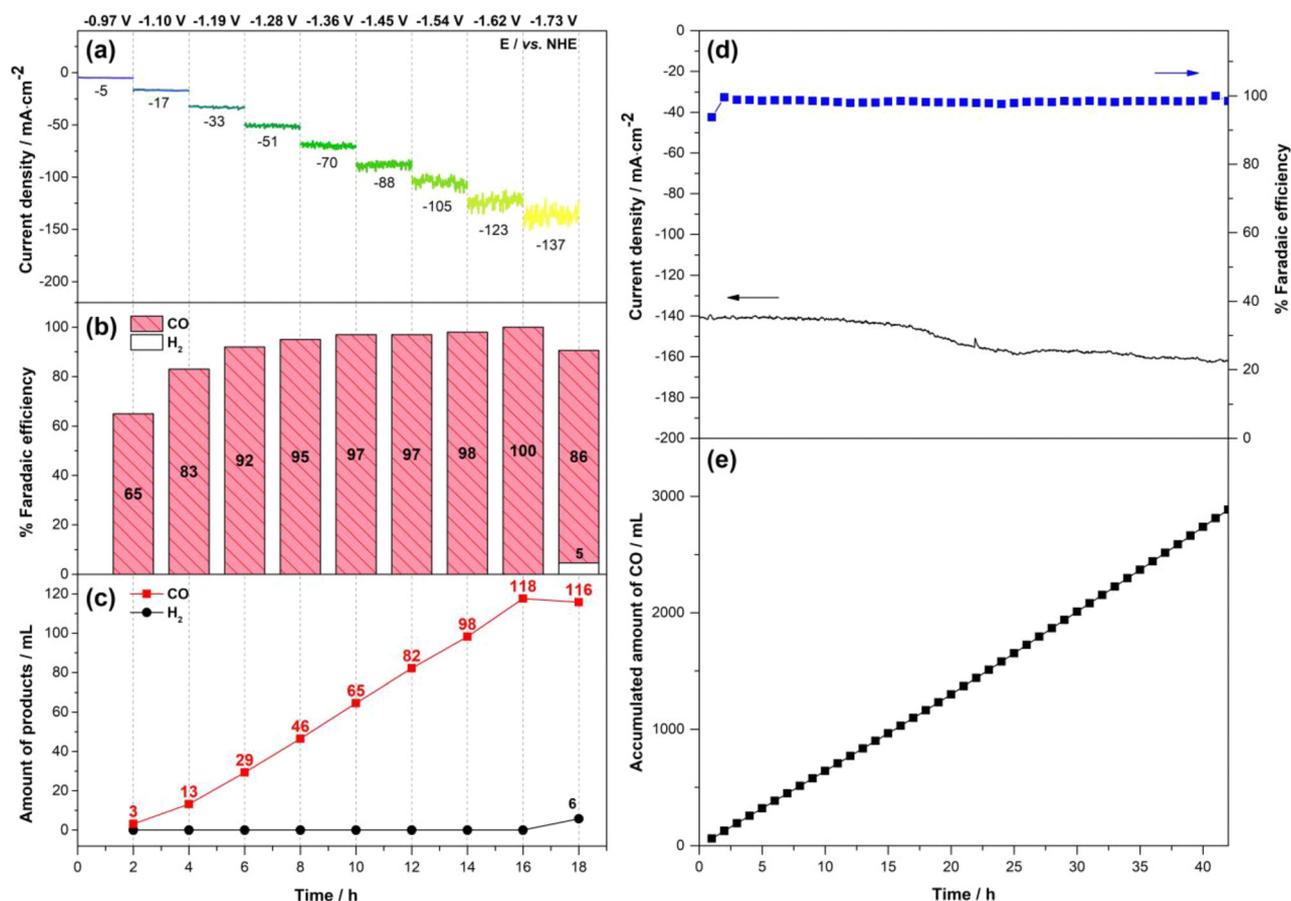

Fig. 7 (a) Chronoamperometric responses, (b) % FE of gas product formation and (c) accumulated amounts of CO (red line) and H_2 (black line) observed in each 2-h interval at various potentials; and (d) chronoamperometric responses with % FE$_{CO}$ and (e) accumulated amount of CO recorded at −1.54 V *vs.* NHE over 42 h of the **p(CoPc-1α)**-catalyzed ECO_2R in the flow cell.

This journal is © the Owner Societies 2026

Phys. Chem. Chem. Phys., 2026, **28**, 3915–3928 | **3921**

ECO$_2$R at the cathode, which migrated through the AEM to recombine with protons (H$^+$) produced from water oxidation at the anode consistent with this ion flux, and we observed a decrease in the catholyte volume, while the anolyte volume increased during extended operation. At a high CO production rate, OH$^-$ transport became rate-limited, leading to OH$^-$ accumulation and subsequent reaction with CO$_2$ at the GDE to form HCO$_3^-$/CO$_3^{2-}$.[62–66] This resulted in an ionic strength increase and thus lowered electrolyte resistance, as observed during the CPE, causing the current density to rise over time. Simultaneously, KHCO$_3$/K$_2$CO$_3$ precipitated within the porous GDE, promoting the leakage and impeding CO$_2$ transport to the catalytic sites.[67–72] Consequently, mass-transport limitations became intensified and the Fe$_{CO}$ declined.

When compared to the published ECO$_2$R flow system catalyzed by a tetraamino-substituted CoPc electropolymer,[24] **p(CoPc-1α)** demonstrated higher FE$_{CO}$ (98% *vs.* 93%) and comparable stability, although with a notably lower TOF (13 *vs.* 140 s^{-1}). Moreover, **p(CoPc-1α)** offered significantly higher current density than the CoPc-based COF reported by Han *et al.*,[60] with similar CO selectivity at slightly more negative potential. Overall, **p(CoPc-1α)** thus presented a well-balanced profile, combining high selectivity, practical current output and decent stability, making it a strong candidate for the scalable electrochemical CO$_2$-to-CO conversion.

3. Theoretical study on charge redistribution and catalytic behavior

In this section, density functional theory (DFT) calculations were performed to investigate the interfacial and interlayer charge redistribution of **CoPc-1α** and **p(CoPc-1α)** on the CFP substrate (Fig. 8). The optimized structures exhibited good
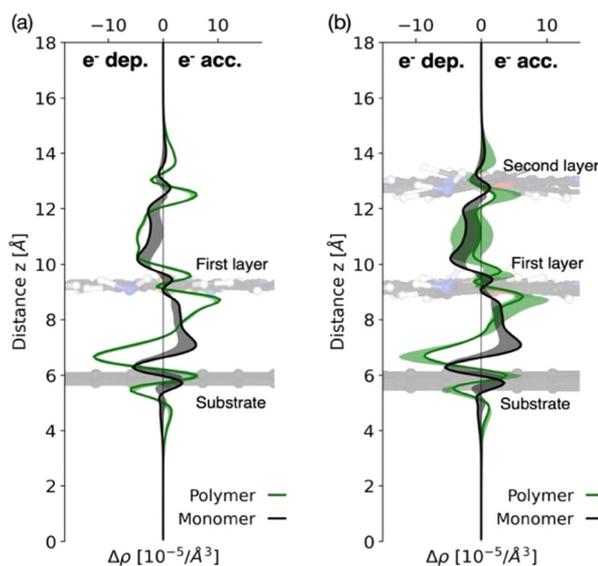

Fig. 8 Planar average of a charge density difference profile in the direction perpendicular to the planes for (a) monolayer and (b) bilayer models for **CoPc-1α** (black) and **p(CoPc-1α)** (green) deposition.

lattice matching between the polymer network (22.3 Å × 22.3 Å) and the graphene surface with the most stable configuration found at the hollow site with a 75° orientation, consistent with favorable π–π stacking interaction (Fig. S15–S19, SI). The planar-averaged charge density difference ($\Delta\rho_{xy}$) profiles revealed distinct electronic characteristics between the two systems. In the monomeric one, electron accumulation occurred mainly at the interface between the CoPc macrocycle and graphene, indicating charge transfer from the substrate to the molecules. In contrast, the polymeric network showed pronounced charge accumulation near the two CoPc layers and diminished substrate interaction, suggesting that the PNZ linkages promoted electron delocalization in the polymer layers and enhanced through-plane electronic coupling. This theoretical observation agreed well with the VF-SWV results, demonstrating efficient charge transport through the Co, Pc and PNZ redox centers. Redistribution of the electron density around the Co and PNZ sites accounted for the experimentally observed Co^{II}/Co^I and PNZ/PNZH$_2$ reduction peaks at −0.28 V and −0.06 V *vs.* NHE, respectively, as well as enhanced conductivity of the **p(CoPc-1α)** film. Furthermore, the results were consistent with those of our previous mechanistic studies presenting the crucial role of the Co^I redox center in a key [Co^I–Pc^{2-}]$^-$ intermediate during the ECO$_2$R.[23] Overall, electropolymerization converted the localized interfacial charge of **CoPc-1α** into a vertically delocalized PNZ-conjugated CoPc network in **p(CoPc-1α)**, thereby facilitating electron transfer while preserving weak substrate binding. This aligned with the high film stability and sustained catalytic current observed in both H-cell and flow-cell experiments.

To gain mechanistic insights into the catalytic pathway of the **p(CoPc-1α)**-catalyzed ECO$_2$R and the effect of the α-functionalization on the Pc macrocycle, computed free-energy (ΔG) profiles for CO$_2$-to-CO conversion catalyzed by **CoPc-1α** in comparison with our previously reported **CoPc-1β** were examined as shown in Fig. 9. The reaction started with the Co^{II}/Co^I reduction, followed by CO$_2$ adsorption on the Co^I center with a small adsorption energy of 0.18 eV, forming a bent *CO$_2$ intermediate stabilized by π-back-donation from metal 3d orbitals. During the CO$_2$ adsorption, the electron transfer upon CO$_2$ activation was not localized only on the Co center. Instead, a substantial fraction of the transferred charge was delocalized over the conjugated π-system of the phthalocyanine macrocycle, indicating that the phthalocyanine macrocyclic ligand functioned as an electronic reservoir that buffers charge during the catalysis (Fig. S20, SI). Subsequent protonation to yield a *COOH intermediate was a rate-determining step, with a slightly lower energy barrier for **CoPc-1α** (3.07 eV) than for **CoPc-1β** (3.19 eV), indicating higher catalytic competence of **CoPc-1α**. Formation of *CO and the following desorption were both downhill in energy, indicating thermodynamically favorable CO release. These theoretical results were consistent with experimental observations showing that **p(CoPc-1α)** exhibited higher CO selectivity and slightly lower overpotential compared to **p(CoPc-1β)**. The α-functionalization on the Pc macrocycle therefore played a crucial role in strengthening metal–ligand electronic communication, promoting charge transfer and lowering the activation energy for the electrochemical CO$_2$-to-CO

3922 | *Phys. Chem. Chem. Phys.*, 2026, **28**, 3915–3928

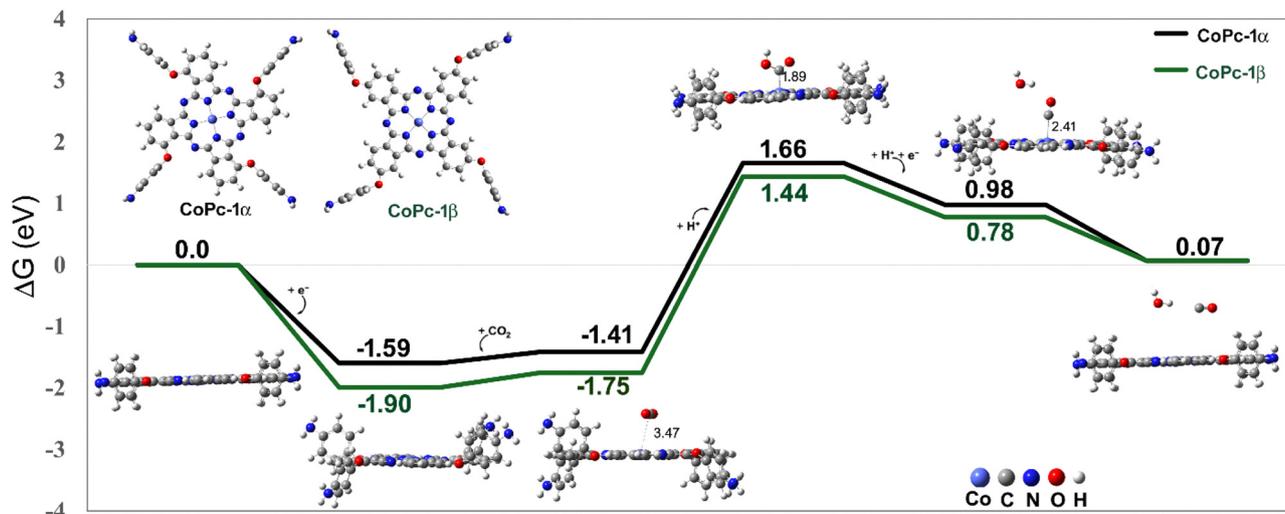This journal is © the Owner Societies 2026

Fig. 9 Comparative ΔG profile of CO_2-to-CO conversion under catalysis of **CoPc-1α** and **CoPc-1β**

conversion. The calculated stacking configuration (Fig. S15–S19, SI) indicated that the distance between the CoPc macrocycles in the first **p(CoPc-1α)** film layer and the carbon-based substrate was 3.30 Å, while the interplanar distance between adjacent CoPc units within the polymer bulk was 3.77 Å. Both values were slightly larger than those obtained for the previously reported **p(CoPc-1β)** analogue, i.e. 3.27 and 3.59 Å, respectively.[25] These data agreed with the previously reported data showing that α-alkoxy substitution on the Pc macrocycles effectively suppressed the aggregation,[73] thereby promoting the accessibility to the catalytically active sites during the ECO_2R. The same study further reported that the α-alkoxy groups could induce a Q-band redshift by narrowing the highest occupied molecular orbital (HOMO)–lowest unoccupied molecular orbital (LUMO) gap. In line with this study, the Q-bands of the **p(CoPc-1α)** film were observed at 643 and 715 nm, redshifted relative to those of the **p(CoPc-1β)** one (631 and 700 nm).[22]

4. Conclusions

The desirable α-tetrasubstituted monomer **CoPc-1α** was successfully synthesized and electropolymerized to form the polymer film of **p(CoPc-1α)** on the ITO-glass, Au-glass, CP and MPL-CFP substrates. The formation of the **p(CoPc-1α)** films was confirmed by UV-vis spectrophotometry, Raman and ATR-FTIR spectroscopy, and SEM-EDX analysis. ATR-FTIR spectroscopy showed the characteristic signals corresponding to the newly formed PNZ linkage in the polymer network, while VF-SWV indicated the efficient intermacrocyclic electron transfer facilitated by the PNZ bridge. At a potential of −1.15 V vs. NHE in the H-cell, **p(CoPc-1α)** demonstrated the optimal catalytic performance by giving the current density, FE_{CO}, TON_{CO} and TOF_{CO} of 38 mA cm^{-2}, 97%, 6.0×10^4 and 0.37 s^{-1}, respectively, for at least 45 h. Compared with its β-tetrasubstituted analog **CoPc-1β**, **CoPc-1α** exhibited higher solubility in DMF and, according to the ICP-OES, the catalyst loading of **p(CoPc-1α)** was approximately twice that of

p(CoPc-1β) on the CP. As a result, the more hindered CO_2 diffusion possibly occurred in **p(CoPc-1α)** led to lower current density and TOF_{CO} observed in the H-cell, despite achieving higher FE_{CO} at the lower reduction potential, compared to the case of **p(CoPc-1β)**. When used in the flow cell, **p(CoPc-1α)** exhibited high catalytic activity for the CO_2-to-CO conversion by giving a current density of 151 mA cm^{-2} with 97% FE_{CO} for 42 h, corresponding to TON_{CO} and TOF_{CO} of 1.9×10^6 and 13 s^{-1}, respectively. The DFT calculations confirmed efficient charge transport through the Co, Pc and PNZ redox centers and revealed that the ECO_2R under catalysis of **CoPc-1α** had a lower energy barrier for the rate determining step than that catalyzed by **CoPc-1β**, reflecting the beneficial effect of the α-substitution of the Pc macrocycles.

5. Experimental

5.1 Materials and methods

All chemicals were purchased from commercial sources and used without further purification, unless noted otherwise. The CPs (AvCarb MGL190), CFPs (avcarb-gds3250) and Nafion membranes (117) were supplied by Fuel Cell Store (USA). The ITO-glass was purchased from Semiconductor wafer, Inc. The Sustainion® X37-50 Grade RT AEM was supplied by dioxide materials, and polytetrafluoroethylene (PTFE) 60 wt% dispersion in water and the Pt wire with a purity of 99.99% were obtained from Sigma Aldrich. ^{1}H- and ^{13}C-NMR spectra were recorded in CDCl$_3$ using a Bruker Avance 400 operated at 400 MHz and 100 MHz, respectively. Chemical shifts (δ) are reported in parts per million (ppm) relative to residual CHCl$_3$ peaks (δ = 7.26 ppm and 77.16 ppm for ^{1}H- and ^{13}C-NMR spectroscopy, respectively). Mass spectra were obtained by HR-MALDI-TOF mass spectrometry (HR-MALDI-TOF-MS). The absorption spectra were measured in DMF at room temperature using an Agilent Cary 60 UV-vis spectrophotometer, and molar extinction coefficients (ε) were reported in L mol^{-1} cm^{-1}. The ATR-FTIR spectra were recorded using s a

This journal is © the Owner Societies 2026

Phys. Chem. Chem. Phys., 2026, **28**, 3915–3928 | **3923**

Nicolet iS50-ATR spectrometer (Thermo Fisher Scientific, U. S.). Raman measurements were conducted at room temperature using a Horiba LabRAM HR800 micro-Raman spectrometer with a 633 nm line of a He–Ne laser. All Raman spectra were calibrated with a signal of a silicon wafer in the Raman spectrum, which typically shows a peak at 520.7 nm. The SEM-EDX images were obtained using a JEOL JSM-IT100. The amount of cobalt on polymeric catalysts was determined through the ICP-OES analysis using a Thermo iCAP 6500 Duo (Thermospectrometer Scientific). The electrochemical experiments were performed using a Metrohm-mAutolab/PGSTAT101 potentiostat with NOVA software and an AMETEK, Inc, VersaSTAT3 potentiostat with VersaStudio software. The flow rate of 99.995% pure CO_2 gas was controlled using a BRONKHORST select mass flow controller (EL-FLOW Select series). The reduction products in the gas phase were determined using an Agilent 8890 GC system equipped with a thermal conductivity detector (TCD) and two parallel columns (CP-Molsieve 5 Å and CP-PoraBOND Q). These columns separated and quantified the gas mixture, including H_2, O_2, N_2, CO, and CO_2, in a single run. Mixtures of each standard gas with N_2 were used for calibration. Ultra-high purity helium (99.999%) was used as a carrier gas for CO and H_2 analysis, respectively.

5.2 Synthesis of 3-(4-nitrophenooxy)phthalonitrile (1)

Following a reported procedure[31] with modification of the types of staring materials and purification conditions, a mixture of 3-nitrophthalonitrile (514 mg, 2.97 mmol), 4-nitrophenol (426 mg, 3.06 mmol), potassium carbonate (399 mg, 2.89 mmol) and dimethylformamide (DMF) (7 mL) was heated at 60 °C for 24 h under a N_2 atmosphere. After cooling to room temperature, the reaction mixture was poured into cold water (50 mL). The resulting precipitate was collected by suction filtration, then washed with water and dried in a vacuum oven at 60 °C for 24 h, affording 3-(4-nitrophenoxy)phthalonitrile (1) as a white solid (723 mg, 92%). m.p. 177–178 °C, ^{1}H NMR (CDCl$_3$) (δ): 8.36–8.31 (m, 2H), 7.77–7.69 (m, 1H), 7.64 (dd, J = 7.7, 1.0 Hz, 1H), 7.29 (dd, J = 8.7, 1.1 Hz, 1H), 7.23–7.17 (m, 2H); ^{13}C NMR (CDCl$_3$) (δ): 159.6, 158.5, 145.0, 135.1, 129.2, 126.6, 123.0, 119.6, 118.0, 112.1, 108.3. Anal. calcd for $C_{14}H_7N_3O_3$: C, 63.40; H, 2.66; N, 15.84. Found: C, 62.32; H, 2.44; N, 15.08.

5.3 Synthesis of 1,8,15,22-tetra(4-nitrophenoxy)phthalocyaninatocobalt(II) (CoPc-2α)

Following a reported procedure[32] with modification of types of staring materials and the purification process, a solution of 3-(4-nitrophenoxy)phthalonitrile (1, 239 mg, 0.225 mmol) and Co(OAc)$_2$·4H$_2$O (131 mg, 0.53 mmol) in DMAE (5.0 mL) in the presence of DBU (0.5 mL) was refluxed under a N_2 atmosphere for 4 h. After cooling to room temperature, the precipitate was collected by centrifugation at 4500 rmp for 5 min and washed by sonication–centrifugation in water (40 mL) and ethanol (40 mL) twice. The resulting precipitate was dried in a vacuum oven at 60 °C for 24 h to afford **CoPc-2α** as a dark green solid (115 mg, 46%). UV-vis: λ_{abs} (ε) 610 (9.3 × 10^4), 672 (8.8 × 10^4) nm; HR-MALDI-TOF m/z (%): found, 1119.1291 [M$^+$]; calcd, 1119.1284 (M$^+$, M = $C_{56}H_{28}CoN_{12}O_{12}$).

5.4 Synthesis of 1,8,15,22-tetra(4-aminophenoxy)phthalocyaninatocobalt(II) (CoPc-1α)

Following a reported procedure[33] with modification of types of staring materials and purification conditions, a suspension of **CoPc-2α** (101 mg, 0.091 mmol) in ethanol (16.0 mL) was slowly treated with a mixture of SnCl$_2$ (5.0 g, 0.03 mmol) in concentrated HCl (7.0 mL) at room temperature under a N_2 atmosphere. After 20 h, the reaction mixture was filtered by a filter paper and the resulting dark blue crude was dissolved in a 1.75 M acetic acid aqueous solution (150 mL). Then, a 0.008 M ammonium hydroxide aqueous solution (40 mL) was added. The resulting dark green precipitate was collected by centrifugation at 4500 rmp for 5 min and washed by sonication–centrifugation in water (40 mL) and ethanol (40 mL) twice. After drying in a vacuum oven at 60 °C for 24 h, **CoPc-1** was obtained as a dark green solid (84 mg, 93%). UV-vis: λ_{abs} (ε) 633 (2.2 × 10^4), 702 (6.4 × 10^4) nm; HR-MALDI-TOF m/z (%): found, 999.2314 [M$^+$]; calcd, 999.2314 (M$^+$, M = $C_{56}H_{36}CoN_{12}O_4$).

5.5 Electropolymerization of CoPc-1α

The ITO-glass substrate was cut into 0.8 cm × 4.0 cm pieces and cleaned by consecutive sonication in toluene, acetone, isopropanol and deionized water. The Au-glass substrate was cut into 1.0 cm × 1.0 cm pieces and cleaned by sonication in acetone. The CP was cut into 1.0 cm × 2.0 cm pieces and cleaned by sonication in acetone. The MPL-CFP substrate was prepared according to a previously reported procedure.[24] After the cleaning process, all substrates were dried in an oven at 100 °C for 15 min. The electrochemical polymerization of **CoPc-1α** was performed in a one-compartment three-electrode system by means of CV. The electrochemical cell consisted of the ITO-glass, Au-glass, CP or MPL-CFP substrates as the WE, the Pt wire as the CE and the Ag/AgCl as QRE. The Ag/AgCl QRE was calibrated using a ferrocene/ferrocenium (Fc/Fc$^+$) redox couple in a 0.1 M TBAPF$_6$ solution in DMF as an external standard. A standard potential of 0.72 V $vs.$ NHE in DMF for the Fc/Fc$^+$ couple was used to convert the potentials recorded against the Ag/AgCl QRE to the NHE scale.[74] The electropolymerization of **CoPc-1α** was conducted in a 1.0 mM **CoPc-1α** solution in DMF containing 0.1 M TBAPF$_6$ under a N_2 atmosphere. The potential was swept in a range from −0.33 V to 1.27 V $vs.$ NHE at a scan rate of 50 mV s^{-1} for 80, 50, 10 and 40 cycles on the ITO-glass, the Au-glass, the CP and the MPL-CFP substrates, respectively. For the catalytic performance studies, the deposited coverage area on the CP and the MPL-CFP substrates was controlled at 1.0 cm × 1.0 cm. After the electropolymerization of **CoPc-1α**, the resulting polymer films were washed with DMF to remove the excess monomer and electrolyte salt, and then dried in an oven at 60 °C for 24 h.

5.6 Determination of the Co content in p(CoPc-1α) on substrates

The Co content in the polymer films was determined by ICP-OES following a previously reported procedure.[75] The polymer samples were digested using a 9 : 1 volume ratio of 65% aqueous

3924 | *Phys. Chem. Chem. Phys.*, 2026, **28**, 3915–3928

This journal is © the Owner Societies 2026

HNO$_3$:30% v/v H$_2$O$_2$ in a 45-mL Teflon-lined autoclave and heated at 185 °C for 5 h. Co standard solutions for the ICP were prepared at suitable concentrations using Milli-Q water and filtered through 0.22 μm nylon membrane filters before measurement.

5.7 Study on electrocatalytic performance of CoPc-1α for the ECO$_2$R

The electrocatalytic activity of **CoPc-1α** was studied using the CV and CPE in both H-cell and flow cell electrochemical setups. The H-cell consisted of a 50-mL two-compartment three-electrode system with the cathodic and anodic chambers separated from each other by an activated proton exchange membrane (Nafion 117).[23] The cathodic chamber contained **p(CoPc-1α)**/CP as the WE and commercial Ag/AgCl (saturated KCl) as the RE, while the anodic chamber contained a Pt wire as the CE. The CV experiments were conducted in N$_2$- and CO$_2$-saturated 0.5 M KHCO$_3$ electrolyte solution in Milli-Q water (45 mL). For the potential optimization experiment, the CPE was performed at the potential ranging between −0.80 V and −1.35 V vs. NHE with 0.05 V increments for 2 h at each potential. CO$_2$ was continuously purged through a catholyte solution at a flow rate of 5 mL min^{-1}. For a long-term stability study, a constant potential of −1.15 V or −1.20 V vs. NHE was applied, and the solutions in both chambers were stirred at 250 rpm during the entire experiment. In the H-cell experiments, the potentials were converted to the NHE scale using the following equation.[74]

$$E_{NHE} = E_{Ag/AgCl\,(saturated\,KCl)} + 0.197$$

The flow cell consisted of three customized PTFE plates stacked and tightened together with the silicone rubber sheets, stainless steel bolts and nuts, followed by configuration as described in the previous work.[24] In the cathodic chamber, the **p(CoPc-1α)**/MPL-CFP connected to a titanium (Ti) plate current collector and the commercial Ag/AgCl (saturated KCl) were used as the WE and RE, respectively. The Pt wire connected to another Ti plate current collector served as the CE and put in the anodic chamber. Both chambers were separated by the Sustainion® X37-50 Grade RT membrane. The 1.0 M KHCO$_3$ electrolyte solution in Milli-Q water was circulated between each chamber and its external 250-mL electrolyte reservoir at a flow rate of 15 mL min^{-1} using a peristaltic pump. CO$_2$ was continuously supplied from a backside of the GDE through a serpentine flow field with a flow rate of 15 mL min^{-1}. For the potential optimization experiment, the potentials ranging from −0.97 V to −1.73 V vs. NHE were applied with 0.05 V increments for 2 h at each potential. For the stability test, the constant potential of −1.54 V vs. NHE was applied with 80% iR compensation and converted to the NHE scale using the following equation.[74]

$$E_{NHE} = E_{Ag/AgCl\,(saturated\,KCl)} + 0.197 - (0.8) \times iR_u$$

where i is the average current and R_u is the solution resistance. Resistance of approximately 7–8 ohms was observed during the experiments.

To conduct online gas product analysis, headspace gas samples (200 μL) were collected from the cathodic chamber of the H-cell or from the cathodic reservoir of the flow cell, and real-time analyzed by the GC every 20 min throughout the experiment.

5.8 VF-SWV study

The electrochemical behavior of **p(CoPc-1α)** was first examined in the one-compartment three-electrode electrochemical setup consisting of **p(CoPc-1α)**/CP, Ag/AgCl (saturated KCl) and a Pt wire as the WE, RE and CE, respectively. The Ar-saturated 0.1 M KOH solution in Milli-Q water (20 mL) was used as the electrolyte. The cyclic voltammogram of the **p(CoPc-1α)** film was recorded by sweeping the potential between −0.90 V and 0.40 V vs. NHE at a scan rate of 100 mV s^{-1}. The VF-SWV experiment of **p(CoPc-1α)**/CP was carried out using a previously reported procedure[56,57,76] in the same one-compartment three-electrode electrochemical setup. The potential between −0.90 V and 0.40 V vs. NHE was applied using a perturbation amplitude and staircase steps of 25 mV and 10 mV. The perturbation frequency (f) was varied from 1250 Hz to 0.33 Hz, corresponding to pulse times from 0.4 μs to 1.5 s. A second-order Savitzky–Golay digital filter of seven points was applied to smoothen the signal in the low-frequency region.

5.9 Electrochemical impedance spectroscopy (EIS)

Following the previously reported procedure.[77] electrochemical impedance spectroscopy (EIS) was performed in the 0.5 M KHCO$_3$ aqueous electrolyte solution in the one-compartment electrochemical cell containing **p(CoPc-1α)**/CP, Ag/AgCl (sat. KCl), and a Pt wire as the WE, RE and CE, respectively. After purging of CO$_2$ into the electrolyte solution for 15 min, the EIS spectra were recorded at −0.95 V vs. NHE with the frequency ranging from 0.1 Hz to 100 000 Hz and an AC voltage of 5 mV on Versastat3.

5.10 Computational details

The theoretical investigations were conducted within the DFT using GPAW software.[78] The projector augmented wave (PAW) method[79] was used to represent core electrons, while the Perdew–Burke–Ernzerhof (PBE) functional[80] was selected for the exchange–correlation functional. To consider the dispersion correction, the Grimme's DFT-D3[81] method was applied. The real space grid was set to (192, 192, 96) throughout the calculations, while energy cutoff for wavefunctions was set to 450 eV. Periodic boundary condition was imposed to reproduce the 2D-graphene substrate where the z axis of the simulation box was set to 18 Å throughout the calculations. K-point sampling was done only at the Γ point. Dipole correction was considered in the z-direction to treat asymmetric stacking along the z-direction. To ensure the localization of the 3d orbital as well as the magnetic moment of the Co 5atom, the Hubbard U correction was imposed with $U = 6.0$ eV to the 3d orbital, following the previous study.[82,83]

In this study, the adsorption energy E_{ads} was described by the equation.

$$E_{ads} = E_{system} - \sum_f E_f \qquad (1)$$

where E_{system} is the total energy of the complex system and E_f is the energy of each fragment, the substrate and each stacking layer. Similarly, charge density difference (CDD) $\Delta\rho_{xy}$ was calculated from a difference between the planar (xy-plane) average of charge density from the total system $\rho_{system,xy}$ subtracted by charge density of each stacking layer $\rho_{f,xy}$, following the equation below.

$$\Delta\rho_{xy} = \rho_{system,xy} - \sum_f \rho_{f,xy} \qquad (2)$$

To construct the ΔG profiles of the CO_2-to-CO conversion on **CoPc-1α**, its molecular model was employed. All quantum chemical calculations were carried out using the Gaussian 16 software package. Geometry optimizations were performed with the B3LYP exchange–correlation functional and the 6-31G(d,p) basis set. No symmetry constraints were imposed on the structures. Subsequent frequency analyses were carried out at the 6-311++G(d,p) level to obtain thermochemical corrections and ΔG. The ΔG of the proton–electron pair ($H^+ + e^-$) was referenced to one-half of the total energy of an isolated H_2 molecule following the computational hydrogen electrode (CHE) approach proposed by Noskov.[84]

Author contributions

Kornkamol Mangmoon: writing – original draft, data curation, investigation, and visualization. Permsak Chairat: writing – original draft, data curation, investigation, and methodology. Yijiao Jiangb: validation. Poobodin Mano and Supawadee Namuangruk: writing – data curation and investigation. Patchanita Thamyongkit: writing – review and editing, resources, supervision, validation, and project administration.

Conflicts of interest

There are no conflicts to declare.

Data availability

The data supporting this article have been included as part of the supplementary information (SI). Supplementary information: the characterization data of the target monomers and polymer films, an H-cell configuration, the electrochemical and catalytic performance data of the H and the flow cells, the theoretical calculation data, the ICP-OES data, and the comparison table of the catalytic performance. See DOI: https://doi.org/10.1039/d5cp04205d.

Acknowledgements

References

1 L. J. R. Nunes, *Environments*, 2023, **10**, 66.

2 K. Wiranarongkorn, K. Eamsiri, Y.-S. Chen and A. Arpornwichanop, *J. CO₂ Util.*, 2023, **71**, 102477.

3 A. Kumar, L. M. Aeshala and T. Palai, *J. Appl. Electrochem.*, 2023, **53**, 1295–1319.

4 Q. Chen, P. Tsiakaras and P. Shen, *Catalysts*, 2022, **12**, 1348.

5 J. Shen, M. J. Kolb, A. J. Göttle and M. T. M. Koper, *J. Phys. Chem. C*, 2016, **120**, 15714–15721.

6 A. Kumar, G. Zhang, W. Liu and X. Sun, *J. Electroanal. Chem.*, 2022, **922**, 116799.

7 Z. Zhang, J. Xiao, X.-J. Chen, S. Yu, L. Yu, R. Si, Y. Wang, S. Wang, X. Meng, Y. Wang, Z.-Q. Tian and D. Deng, *Angew. Chem., Int. Ed.*, 2018, **57**, 16339–16342.

8 S. Yu, D. Menga, A. Moranka, S. Muy, M. Busch, V. Tileli and Y. Shao-Horn, *J. Am. Chem. Soc.*, 2025, **147**, 34183–34198.

9 L. Yao, J. Ding, X. Cai, L. Liu, N. Singh, C. C. L. McCrory and B. Liu, *ACS Nano*, 2024, **18**, 21623–21632.

10 Q. Feng, Y. Sun, X. Gu and Z. Dong, *Electrolysis*, 2022, **13**, 675–690.

11 Y.-H. Tse, P. Janda, H. Lam, J. Zhang, W. J. Pietro and A. B. P. Lever, *J. Porphyrins phthalocyanines*, 1997, **01**, 3–16.

12 S. Meshitsuka, M. Ichikawa and K. Tamaru, *J. Chem. Soc., Chem. Commun.*, 1974, 158–159, DOI: 10.1039/C39740000158.

13 X. Zhang, Z. Wu, X. Zhang, L. Li, Y. Li, H. Xu, X. Li, X. Yu, Z. Zhang, Y. Liang and H. Wang, *Nat. Commun.*, 2017, **8**, 14675.

14 H. Yang, M. Driess and P. W. Menezes, *Adv. Energy Mater.*, 2021, **11**, 2102074.

15 M. Asad, A. Shah, F. J. Iftikhar, R. Nimal, J. Nisar and M. A. Zia, *Sustainable Chem.*, 2022, **3**, 286–299.

16 G. Barati Darband, M. Aliofkhazraei and A. S. Rouhaghdam, *J. Colloid Interface Sci.*, 2019, **547**, 407–420.

17 M. Josowicz and J. Janata, in *Applications of Electroactive Polymers*, ed. B. Scrosati, Springer Netherlands, Dordrecht, 1993, pp. 310–343, DOI: 10.1007/978-94-011-1568-1_10.

18 A. Pailleret and F. Bedioui, in *N4-Macrocyclic Metal Complexes*, ed. J. H. Zagal, F. Bedioui and J.-P. Dodelet, Springer New York, New York, NY, 2006, pp. 363–438, DOI: 10.1007/978-0-387-28430-9_8.

19 L. Liu, in *Solution-Processed Organic Light-emitting Devices*, ed. G. Xie, Woodhead Publishing, 2024, pp. 477–494, DOI: 10.1016/B978-0-323-95146-3.00004-5.

20 H. A. Abd El-Rahman and H. H. Rehan, *J. Appl. Electrochem.*, 1993, **23**, 827–834.

21 T. Shimidzu, *React. Polym., Ion Exch., Sorbents*, 1987, **6**, 221–227.

22 M. Ando, Y. Watanabe, T. Iyoda, K. Honda and T. Shimidzu, *Thin Solid Films*, 1989, **179**, 225–231.

23 J. Luangchaiyaporn, D. Wielend, D. Solonenko, H. Seelajaroen, J. Gasiorowski, M. Monecke, G. Salvan, D. R. T. Zahn,

3926 | *Phys. Chem. Chem. Phys.*, 2026, **28**, 3915–3928

This journal is © the Owner Societies 2026

N. S. Sariciftci and P. Thamyongkit, *Electrochim. Acta*, 2021, **367**, 137506.

24 J. Luangchaiyaporn, P. Chairat, R. Sodkhomkhum, N. S. Sariciftci and P. Thamyongkit, *ChemCatChem*, 2024, **16**, e202400281.

25 P. Chairat, J. Luangchaiyaporn, A. S. Kochubei, A. N. Marianov, P. Mano, S. Namuangruk, Y. Jiang and P. Thamyongkit, *ChemSusChem*, 2025, **18**, e202501266.

26 A. W. Snow, in *The Porphyrin Handbook*, ed. K. M. Kadish, K. M. Smith and R. Guilard, Academic Press, Amsterdam, 2003, pp. 129–176, DOI: 10.1016/B978-0-08-092391-8.50009-1.

27 R. R. Cranston and B. H. Lessard, *RSC Adv.*, 2021, **11**, 21716–21737.

28 C. G. Claessens, U. Hahn and T. Torres, *Chem. Rec.*, 2008, **8**, 75–97.

29 N. Kobayashi, H. Ogata, N. Nonaka and E. A. Luk'yanets, *Chem. – Eur. J.*, 2003, **9**, 5123–5134.

30 T. Ikeuchi, J. Mack, T. Nyokong, N. Kobayashi and M. Kimura, *Langmuir*, 2016, **32**, 11980–11985.

31 B. Amir, H. Zhou, F. Liu and H. Aurangzeb, *J. Polym. Sci., Part A: Polym. Chem.*, 2010, **48**, 5916–5920.

32 N. Hamdi, R. Medyouni, H. Bilel, L. Mansour and A. Romerosa, *Molecules*, 2017, **22**, 605.

33 D. Wöhrle and V. I. Bregadze, *J. Porphyrins phthalocyanines*, 2005, **9**, 268–274.

34 Y. Wei, G. W. Jang, C. C. Chan, K. F. Hsueh, R. Hariharan, S. A. Patel and C. K. Whitecar, *J. Phys. Chem.*, 1990, **94**, 7716–7721.

35 K. S. Lokesh and A. Adriaens, *Dyes Pigm.*, 2015, **112**, 192–200.

36 H. Li and T. F. Guarr, *J. Chem. Soc., Chem. Commun.*, 1989, 832–834, DOI: 10.1039/C39890000832.

37 N. Manjunatha, M. Imadadulla, K. S. Lokesh and K. R. Venugopala Reddy, *Dyes Pigm.*, 2018, **153**, 213–224.

38 J. Roncali, A. Yassar and F. Garnier, *J. Chem. Soc., Chem. Commun.*, 1988, 581–582, DOI: 10.1039/C39880000581.

39 R. Georgescu, C. Boscornea, I. Calinescu and R. State, *Rev. Chim.*, 2015, **66**, 1554–1557.

40 K. Serbest, İ. Değirmencioğlu, Y. Ünver, M. Er, C. Kantar and K. Sancak, *J. Organomet. Chem.*, 2007, **692**, 5646–5654.

41 M. Tian, T. Wada and H. Sasabe, *J. Heterocycl. Chem.*, 1997, **34**, 171–176.

42 M. Tian, T. Wada and H. Sasabe, *Dyes Pigm.*, 2002, **52**, 1–8.

43 A. V. Ziminov, S. M. Ramsh, E. I. Terukov, I. N. Trapeznikova, V. V. Shamanin and T. A. Yurre, *Semiconductors*, 2006, **40**, 1131–1136.

44 O. Tsaryova, A. Semioshkin, D. Wöhrle and V. I. Bregadze, *J. Porphyrins Phthalocyanines*, 2005, **09**, 268–274.

45 V. Ahsen, E. Yilmazer, M. Ertas and Ö. Bekâroğlu, *J. Chem. Soc., Dalton Trans.*, 1988, 401–406, DOI: 10.1039/DT9880000401.

46 O. E. Sielcken, M. M. Van Tilborg, M. F. M. Roks, R. Hendriks, W. Drenth and R. J. M. Nolte, *J. Am. Chem. Soc.*, 1987, **109**, 4261–4265.

47 M. Koçak, A. Cihan, A. I. Okur, A. Gül and Ö. Bekaroğlu, *Dyes Pigm.*, 2000, **45**, 9–14.

48 A. Kumar, S. Samanta, S. Latha, A. K. Debnath, A. Singh, K. P. Muthe and H. C. Barshilia, *RSC Adv.*, 2017, **7**, 4135–4143.

49 K. S. Lokesh and A. Adriaens, *Dyes Pigm.*, 2013, **96**, 269–277.

50 M. Tammer, *Colloid Polym. Sci.*, 2004, **283**, 235.

51 C. Stammer and A. Taurins, *Spectrochim. Acta*, 1963, **19**, 1625–1654.

52 R. D. Rodriguez, C. J. Villagómez, A. Khodadadi, S. Kupfer, A. Averkiev, L. Dedelaite, F. Tang, M. Y. Khaywah, V. Kolchuzhin, A. Ramanavicius, P.-M. Adam, S. Gräfe and E. Sheremet, *ACS Photonics*, 2021, **8**, 2243–2255.

53 B. J. Palys, D. M. W. van den Ham, W. Briels and D. Feil, *J. Raman Spectrosc.*, 1995, **26**, 63–76.

54 C. A. Melendres and V. A. Maroni, *J. Raman Spectrosc.*, 1984, **15**, 319–326.

55 Z. Liu, X. Zhang, Y. Zhang and J. Jiang, *Spectrochim. Acta, Part A*, 2007, **67**, 1232–1246.

56 A. N. Marianov, A. S. Kochubei, T. Roman, O. J. Conquest, C. Stampfl and Y. Jiang, *Anal. Chem.*, 2021, **93**, 10175–10186.

57 A. S. Kochubei, A. N. Marianov, O. J. Conquest, T. Lu, Y. Liu, C. Stampfl and Y. Jiang, *J. Mater. Chem. A*, 2025, **13**, 1874–1886.

58 H. Tao, S. Wang, H. Liu and C. Lian, *Angew. Chem., Int. Ed.*, 2025, **64**, e202418447.

59 Y. Niu, H. Tao, J. Li, C. Lian and H. Liu, *J. Phys. Chem. C*, 2025, **129**, 19371–19379.

60 B. Han, X. Ding, B. Yu, H. Wu, W. Zhou, W. Liu, C. Wei, B. Chen, D. Qi, H. Wang, K. Wang, Y. Chen, B. Chen and J. Jiang, *J. Am. Chem. Soc.*, 2021, **143**, 7104–7113.

61 B. Han, Y. Jin, B. Chen, W. Zhou, B. Yu, C. Wei, H. Wang, K. Wang, Y. Chen, B. Chen and J. Jiang, *Angew. Chem., Int. Ed.*, 2022, **61**, e202114244.

62 F. Habibzadeh, P. Mardle, N. Zhao, H. D. Riley, D. A. Salvatore, C. P. Berlinguette, S. Holdcroft and Z. Shi, *Electrochem. Energy Rev.*, 2023, **6**, 26.

63 P. Zhu and H. Wang, *Nat. Catal.*, 2021, **4**, 943–951.

64 S. M. Hosseini, S. S. Madaeni and A. R. Khodabakhshi, *Sep. Sci. Technol.*, 2012, **47**, 455–462.

65 K. Solonchenko, A. Kirichenko and K. Kirichenko, *Membranes*, 2023, **13**, 52.

66 H. J. Kwon, B. Kim, G. Lim and J. Han, *J. Mater. Chem. A*, 2018, **6**, 7714–7723.

67 M. E. Leonard, L. E. Clarke, A. Forner-Cuenca, S. M. Brown and F. R. Brushett, *ChemSusChem*, 2020, **13**, 400–411.

68 D. G. Wheeler, B. A. W. Mowbray, A. Reyes, F. Habibzadeh, J. He and C. P. Berlinguette, *Energy Environ. Sci.*, 2020, **13**, 5126–5134.

69 S. Haj-Bsoul, J. R. Varcoe and D. R. Dekel, *J. Electroanal. Chem.*, 2022, **908**, 116112.

70 S. Willdorf-Cohen, A. Zhegur-Khais, J. Ponce-González, S. Bsoul-Haj, J. R. Varcoe, C. E. Diesendruck and D. R. Dekel, *ACS Appl. Energy Mater.*, 2023, **6**, 1085–1092.

71 Y. Wang, J. Qiu, J. Peng, L. Xu, J. Li and M. Zhai, *J. Membr. Sci.*, 2011, **376**, 70–77.

72 E. Fontananova, D. Messana, R. A. Tufa, I. Nicotera, V. Kosma, E. Curcio, W. van Baak, E. Drioli and G. Di Profio, *J. Power Sources*, 2017, **340**, 282–293.

73 T. Furuyama, K. Satoh, T. Kushiya and N. Kobayashi, *J. Am. Chem. Soc.*, 2014, **136**, 765–776.

74 T. J. Smith and K. J. Stevenson, in *Handbook of Electrochemistry*, ed. C. G. Zoski, Elsevier, Amsterdam, 2007, pp. 73–110, DOI: 10.1016/B978-044451958-0.50005-7.

75 W. Boonta, W. Sangkhun, C. Suppaso, N. Chantanop, W. Panchan, K. Chainok, P. Thamyongkit, T. Sudyoadsuk, K. Maeda, T. Butburee and J. Unruangsri, *ACS Catal.*, 2023, **13**, 12391–12402.

76 A. N. Marianov and Y. Jiang, *Acc. Mater. Res.*, 2022, **3**, 620–633.

77 S. Zhou, L.-J. Zhang, L. Zhu, C.-H. Tung and L.-Z. Wu, *Adv. Mater.*, 2023, **35**, 2300923.

78 J. J. Mortensen, A. H. Larsen, M. Kuisma, A. V. Ivanov, A. Taghizadeh, A. Peterson, A. Haldar, A. O. Dohn, C. Schäfer, E. Ö. Jónsson, E. D. Hermes, F. A. Nilsson, G. Kastlunger, G. Levi, H. Jónsson, H. Häkkinen, J. Fojt, J. Kangsabanik, J. Sødequist, J. Lehtomäki, J. Heske, J. Enkovaara, K. T. Winther, M. Dulak, M. M. Melander, M. Ovesen, M. Louhivuori, M. Walter, M. Gjerding, O. Lopez-Acevedo, P. Erhart, R. Warmbier, R. Würdemann, S. Kaappa, S. Latini, T. M. Boland, T. Bligaard, T. Skovhus, T. Susi, T. Maxson, T. Rossi, X. Chen, Y. L. A. Schmerwitz, J. Schiøtz, T. Olsen, K. W. Jacobsen and K. S. Thygesen, *J. Chem. Phys.*, 2024, **160**, 092503.

79 G. Kresse and D. Joubert, *Phys. Rev. B: Condens. Matter Mater. Phys.*, 1999, **59**, 1758–1775.

80 J. P. Perdew, K. Burke and M. Ernzerhof, *Phys. Rev. Lett.*, 1996, **77**, 3865–3868.

81 S. Grimme, J. Antony, S. Ehrlich and H. Krieg, *J. Chem. Phys.*, 2010, **132**, 154104.

82 S. Bhattacharjee, B. Brena, R. Banerjee, H. Wende, O. Eriksson and B. Sanyal, *Chem. Phys.*, 2010, **377**, 96–99.

83 S. L. Dudarev, G. A. Botton, S. Y. Savrasov, C. Humphreys and A. P. Sutton, *Phys. Rev. B: Condens. Matter Mater. Phys.*, 1998, **57**, 1505–1509.

84 J. K. Nørskov, J. Rossmeisl, A. Logadottir, L. Lindqvist, J. R. Kitchin, T. Bligaard and H. Jónsson, *J. Phys. Chem. B*, 2004, **108**, 17886–17892.

3928 | *Phys. Chem. Chem. Phys.*, 2026, **28**, 3915–3928

This journal is © the Owner Societies 2026